


Combined Photothermal Chemotherapy for Effective Treatment Against Breast Cancer in Mice Model

Junzi Chen*, Yumin Xiang*, Rong Bao, Yuyi Zheng, Yingxi Fang, Jiajia Feng, Di Wu , Xiaojie Chen

Key Laboratory of Neuropharmacology and Translational Medicine of Zhejiang Province, School of Pharmaceutical Sciences, The First Affiliated Hospital of Zhejiang Chinese Medical University (Zhejiang Provincial Hospital of Chinese Medicine), Hangzhou, 310053, People's Republic of China

*These authors contributed equally to this work

Correspondence: Xiaojie Chen; Di Wu, Key Laboratory of Neuropharmacology and Translational Medicine of Zhejiang Province, School of Pharmaceutical Sciences, The First Affiliated Hospital of Zhejiang Chinese Medical University (Zhejiang Provincial Hospital of Chinese Medicine), Hangzhou, People's Republic of China, Email chenxiaojie0902@163.com; wudichem@zju.edu.cn

Introduction: Breast cancer ranks among the most prevalent cancers in women, characterized by significant morbidity, disability, and mortality. Presently, chemotherapy is the principal clinical approach for treating breast cancer; however, it is constrained by limited targeting capability and an inadequate therapeutic index. Photothermal therapy, as a non-invasive approach, offers the potential to be combined with chemotherapy to improve tumor cellular uptake and tissue penetration. In this research, a mesoporous polydopamine-coated gold nanorod nanoplateform, encapsulating doxorubicin (Au@mPDA@DOX), was developed.

Methods: This nanoplateform was constructed by surface coating mesoporous polydopamine (mPDA) onto gold nanorods, and doxorubicin (DOX) was encapsulated in Au@mPDA owing to π - π stacking between mPDA and DOX. The dynamic diameter, zeta potential, absorbance, photothermal conversion ability, and drug release behavior were determined. The cellular uptake, cytotoxicity, deep penetration, and anti-tumor effects were subsequently investigated in 4T1 cells. After that, fluorescence imaging, photothermal imaging and pharmacodynamics studies were utilized to evaluate the anti-tumor effects in tumor-bearing mice model.

Results: This nanoplateform exhibited high drug loading capacity, excellent photothermal conversion and, importantly, pH/photo-thermal dual-responsive drug release behavior. The in vitro results revealed enhanced photothermal-facilitated cellular uptake, drug release and tumor penetration of Au@mPDA@DOX under near-infrared irradiation. In vivo studies confirmed that, compared with monotherapy with either chemotherapy or photothermal therapy, the anti-tumor effects of Au@mPDA@DOX are synergistically improved.

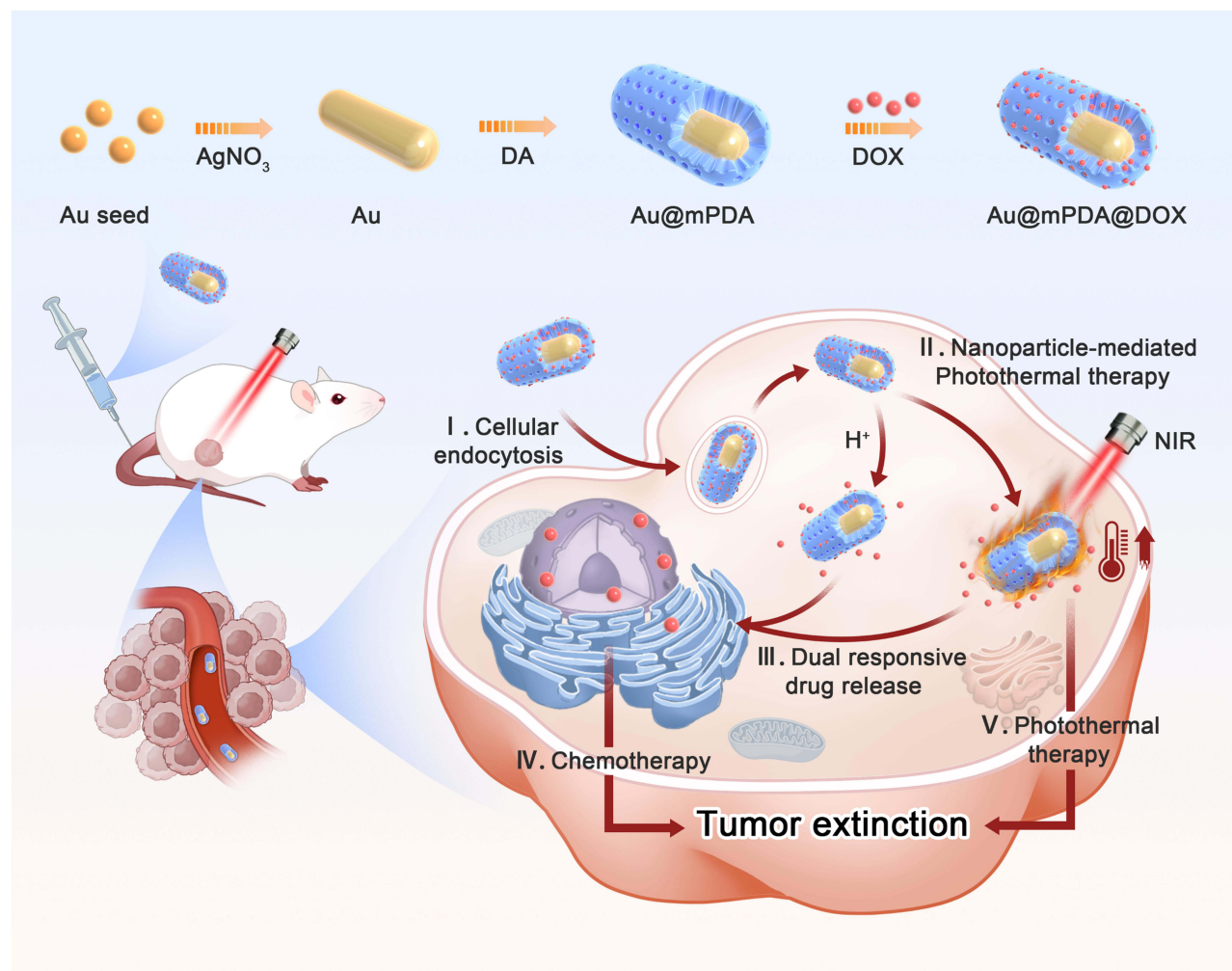
Conclusion: Together with good biosafety and biocompatibility, the Au@mPDA@DOX nanoplateform provides an alternative method for safe and synergistic treatment of breast cancer.

Keywords: breast cancer, synergistic therapy, polydopamine, gold nanorod, chemotherapy

Introduction

Breast cancer is one of the most prevalent cancers among women and accounts for 31% of all new diagnoses, owing to its high morbidity, disability, and mortality.^{1,2} Conventional treatments for breast cancer include surgery, chemotherapy, radiotherapy, etc.³ Overall, chemotherapy is considered the standard strategy for treating breast cancer after surgical intervention. Doxorubicin (DOX), paclitaxel, and fluorouracil are widely utilized for clinical chemotherapy for breast cancer treatment and have good anti-tumor effects.⁴ In particular, DOX is an effective chemotherapeutic agent for suppressing cancer cell growth via interference with DNA replication.^{5,6} However, during long-term blood circulation, DOX molecules with phenolic structures under conventional medication routes can be quickly metabolized in the bloodstream or distributed around the tumor vasculature rather than penetrating into the tumor parenchyma.⁷ Thus, low targeting efficiency requires a high medication dose, which may lead to potential adverse effects, such as

Graphical Abstract



gastrointestinal disorders, cardiac dysfunction, and drug resistance.⁸ Thus, it is imperative to improve drug delivery efficiency to increase therapeutic efficacy and reduce potential adverse effects in the fight against breast cancer.

Nanodrug delivery systems (NDDSs), which can endow therapeutics with increased stability, low toxicity, and enhanced anti-tumor functionalities, have received tremendous attention in cancer therapy.^{9,10} Drug carriers at the nanoscale can passively accumulate at the tumor site via the enhanced permeability and retention (EPR) effect because of the high density and leaky vessels of solid tumors, as well as poor lymphatic drainage.^{11–14} Unfortunately, a majority of NDDSs reach the tumor site and stagnate at the margin between tumor tissues and blood vessels. Tumor penetration of therapeutics into deep sites is severely hampered by limited interstitial fluid flow and a dense tumor interstitial matrix.¹⁵

Owing to the physiological complexity of tumors, monotherapy with chemotherapeutic medication is often limited in cancer treatment. Recently, synergistic therapy has become a novel strategy for cancer treatment by minimizing adverse effects and maximizing therapeutic outcomes through synergistic functions.¹⁶ Numerous strategies, including photothermal therapy (PTT), chemodynamic therapy, and gene therapy, have been utilized in combination with chemotherapy for breast cancer treatment.^{17–19} As a non-invasive and spatiotemporally controlled method, photothermal therapy (PTT) has garnered significant interest in cancer treatment, particularly in breast cancer.^{20,21} Photothermal agents, such as inorganic nanostructures,^{22–24} polymer nanoparticles,^{25–27} carbon

nanomaterials,^{18,28,29} and other functional materials,³⁰ are employed to convert light energy into heat, creating localized hyperthermia to disrupt cancer cells. Among these, gold (Au) nanostructures with customized designs, including Au nanospheres, nanorods, and nanocages, have been extensively studied due to their effective photo-thermal conversion and low toxicity.^{31–33} In particular, Au nanorods (AuNRs) with simple preparation and tunable localized surface plasmon resonance (LSPR) are considered promising candidates for cancer treatment.^{34,35} The elongated shape of the AuNRs led to higher light absorbance in the wavelength region beyond the visible range, enabling PTT at deeper sites in the tumor tissue.^{36–39} Therefore, integrating PTT with chemotherapy into one nanoplatform, which can facilitate cellular uptake and tissue penetration inside solid tumors, is highly desirable for breast cancer treatment.^{40,41}

In this study, a core-shell nanoplatform (gold nanorod@mesoporous polydopamine@doxorubicin, abbreviated as Au@mPDA@DOX) was constructed for combined photothermal chemotherapy against breast cancer in mice model. These hybrid nanoparticles could be obtained by surface coating mussel-inspired mesoporous polydopamine (mPDA) onto AuNRs.^{39,42,43} Importantly, mPDA functionalization significantly improved the DOX loading capacity because of the meso-channels and molecular interactions between mPDA and DOX.⁴⁴ Additionally, the drug of interest can be released in response to either acidic conditions or near-infrared (NIR) irradiation in a controlled manner. In vivo studies have demonstrated that drug-loaded nanoparticles can accumulate in tumors and exert anti-tumor effects through combined therapy. In addition, NIR light has great potential for deep penetration into biological tissues, which is essential for solid tumor treatment. Under NIR irradiation, the nanocarriers show improved tumor penetration, and irradiation synergistically contributes to on-demand drug release. Therefore, this nanoplatform provides a potential optical strategy for synergistic and on-demand therapy in the fight against breast cancer.

Materials and Methods

Hydrogen tetrachloroaurate (III) trihydrate ($\text{HAuCl}_4 \cdot 3\text{H}_2\text{O}$) was obtained from Alfa Aesar (Shanghai, China). Hexadecyl trimethyl ammonium bromide (CTAB), silver nitrate (AgNO_3), hydroquinone, sodium borohydride (NaBH_4), dopamine hydrochloride ($\text{DA} \cdot \text{HCl}$), and Pluronic F127 copolymer were purchased from Sigma-Aldrich (USA). Doxorubicin hydrochloride ($\text{DOX} \cdot \text{HCl}$) was purchased from Yuanye Biological Technology (Shanghai, China). 1,3,5-Trimethylbenzene (TMB) was obtained from Tokyo Chemical Industry Co., Ltd. (Japan). Ammonia aqueous solution ($\text{NH}_3 \cdot \text{H}_2\text{O}$) was purchased from HUSHI (Shanghai, China).

The Synthesis of the Core-Shell Nanoparticles

A seed-mediated growth method was utilized to prepare the Au nanorods according to our previous report with some modifications.⁴³ Briefly, the Au seeds were synthesized via the addition of HAuCl_4 (10 mM) to a CTAB solution (0.1 M) at a volume ratio of 1:20 with vigorous stirring. Then, 10 μL of AgNO_3 was quickly added to the above mixture. The pH of the mixture was adjusted with HCl (1 M) after stirring for 60s, followed by the addition of hydroquinone (0.1 M, 525 μL), and the mixture quickly became colorless. After incubation at 30 °C for 15 min, the mixture was aged for 15 h after the addition of freshly prepared NaBH_4 . The Au nanorods were obtained by centrifugation (20,000 $\times g$, 15 min).

For polydopamine-coated gold nanorod synthesis, equal volumes of $\text{DA} \cdot \text{HCl}$ aqueous solution (15 mg) and F127 ethanol solution (50 mg) were mixed. Then, 60 μL of TMB was quickly added to the mixture with vigorous stirring to form a white turbid liquid. After the addition of the Au nanorods, the mixture was sonicated until the solution became transparent. $\text{NH}_3 \cdot \text{H}_2\text{O}$ was subsequently added to initiate self-polymerization. After continuous stirring for 1 h, the final mixture was centrifuged and washed with water and ethanol at least three times to obtain Au@mPDA. For drug loading, $\text{DOX} \cdot \text{HCl}$ was mixed with the Au@mPDA solution and stirred for 24 h in the dark.

The Morphology and Absorbance Characterization

The morphologies of Au and Au@mPDA were observed via transmission electron microscopy (TEM, Hitachi, Japan) and scanning electron microscopy (SEM, Hitachi, Japan). Elemental mapping and energy dispersive X-ray spectroscopy

(EDS) of the Au@mPDA were performed via transmission electron microscopy (TEM) (JEOL JEM-F200, Japan). The zeta potential was measured via a Malvern Zetasizer (Nano-ZS90, UK). A UV-Vis spectrometer (UH5700, Hitachi, Japan) was used to analyze the absorbance spectra.

In vitro Photothermal Ability Evaluation

An infrared thermal camera was used to evaluate the photothermal ability of Au@mPDA at various concentrations and power densities. Briefly, 1 mL of Au@mPDA solution at various concentrations (10, 25, 50, or 100 $\mu\text{g/mL}$) was irradiated with an 808 nm laser (0.3 W/cm^2 , 5 min), and the temperature change was monitored. Similarly, Au@mPDA (50 $\mu\text{g/mL}$) was irradiated with an 808 nm laser at different power densities (0.3 to 1.2 W/cm^2). The photothermal stability of the Au@mPDA was measured after laser irradiation for 5 min, followed by cooling for 10 min.

In vitro Drug Release Investigation

Drug release profiles of Au@mPDA@DOX were recorded via a dialysis method. Briefly, Au@mPDA@DOX was dialyzed in PBS against a semipermeable membrane (MWCO = 3500 Da) with various pH values of 7.4, 6.2, and 5.0. Under constant stirring at 37 °C, the samples outside the dialysis bag were collected at determined time intervals, and the concentration of DOX was measured via a microplate reader.

Hemolysis Assay

The blood toxicity of the Au@mPDA was measured via a hemolysis assay. Briefly, fresh blood was obtained from female BALB/c mice (5–6 weeks, 20 ± 2 g), which were obtained from Zhejiang Chinese Medical University Laboratory Animal Research Center. All animal study protocols were approved by the Zhejiang Chinese Medical University Laboratory Animal Research Center Ethics Committee (approval number: IACUC-20231023-05). All the animal studies were performed according to the Guidelines for the Care and Use of Laboratory Animals of the Chinese Animal Welfare Committee and were approved by the Institutional Animal Care and Use Committee at Zhejiang Chinese Medical University. Then, the samples were centrifuged, washed several times, and diluted to 2% with saline to form a red blood cell (RBC) solution. Then, the RBC suspension and the various concentrations of the Au@mPDA solution (1 to 100 $\mu\text{g/mL}$) were mixed at a volume ratio of 1:1. After incubation for 1 h, the supernatant was collected, and the absorbance was measured using a microplate reader at 414 nm to evaluate the hemolysis ratio.

In vitro Cellular Uptake Assay

4T1 murine breast cancer cells were obtained from ATCC. 4T1 cells were seeded in 24-well plates at a density of 5×10^4 cells per well. After incubation overnight, the cells were treated with Au@mPDA@DOX (DOX concentration: 10 $\mu\text{g/mL}$) for various durations. The cells in the laser group were irradiated with a laser for 5 min at 2 h of incubation. After being washed with PBS, the cells were fixed and stained with DAPI, followed by fluorescence visualization using a confocal laser scanning microscope (CLSM, FV3000, Olympus, Japan).

In vitro Cytotoxicity Evaluation

4T1 cells were seeded in 96-well plates at a density of 5×10^3 cells per well and cultured overnight. The various concentrations of the DOX, Au@mPDA or Au@mPDA@DOX solutions were subsequently added to the cells. The cells in the laser group were irradiated after 4 h of incubation. After incubation for 24 h, the cell viability was determined via a CCK-8 assay.

Study of Deep Penetration of Tumor Spheroids

4T1 cells were seeded in 96-well ultralow attachment plates for 7 days until three-dimensional (3D) tumor spheroid formation occurred. The 4T1 tumor spheroids were treated with Au@mPDA@DOX for 4 or 8 h, and laser irradiation was conducted after 2 h of incubation. After medium removal and washing with PBS, the tumor spheroids were fixed with paraformaldehyde for 15 min. Fluorescence images at different depths were captured via CLSM in Z-stack mode.

Live Cell Staining Assay

4T1 cells were seeded in glass-bottom culture dishes (2×10^5 cells per well) and incubated overnight. After incubation with PBS, DOX, Au@mPDA, or Au@mPDA@DOX for 6 h, the cells were stained with Calcein AM for 15 min. After that, the cells were washed and then imaged via CLSM.

Cell Apoptosis Assay

Cell apoptosis was assessed using an Annexin V-APC/7-AAD apoptosis kit. In brief, 5×10^4 4T1 cells were plated in 96-well plates and incubated overnight. Subsequently, the cells were exposed to PBS, DOX, Au@mPDA, or Au@mPDA@DOX for 6 h, then collected and stained with Annexin V-APC and 7-AAD. The proportion of apoptotic cells was determined by flow cytometry (CytoFLEX S, Beckman, USA).

In vitro Migration Inhibition Assay

A migration assay was conducted to evaluate the antimetastatic properties. 4T1 cells were plated in 6-well plates (2×10^5 cells per well) and incubated overnight. Scratches were made in the cell monolayers using a 10 μ L pipette tip, and the cells were washed with PBS several times to remove debris. The cells were then treated with PBS, DOX, Au@mPDA, or Au@mPDA@DOX along with laser irradiation for 24 h. After washing three times, the scratches from different treatments were inspected with an optical microscope (Leica, DFC7000T, Germany), and the scratch width was measured using ImageJ.

In vivo and ex vivo Fluorescence Imaging Studies

All animal study protocols received approval from the Zhejiang Chinese Medical University Laboratory Animal Research Center Ethics Committee. Female BALB/c mice (5–6 weeks, 20 ± 2 g) were sourced from the Zhejiang Chinese Medical University Laboratory Animal Research Center. To create 4T1 tumor-bearing mice, 4T1 cells (1×10^6 cells/100 μ L) were injected subcutaneously into the right back of the mice. When the tumor volume surpassed 100 mm³, the mice were intravenously administered indocyanine green (ICG)-labeled Au@mPDA (ICG concentration: 2.5 mg/kg). In vivo fluorescence images were acquired at designated time points using an in vivo imaging system (IVIS, PerkinElmer, USA). Following 24 h of imaging, the major organs and tumors were harvested for ex vivo imaging. Tumor sections were embedded, sliced, and stained with DAPI, with CD31 assessed using CLSM.

In vivo Anti-Tumor Study

The 4T1 tumor-bearing mice were divided into saline (control), DOX, Au@mPDA, Au@mPDA@DOX, Au@mPDA + laser, or Au@mPDA@DOX + laser groups and treated with the corresponding drugs. The Au@mPDA + laser or Au@mPDA@DOX groups were treated with 808 nm laser irradiation 2 h post-injection, and then, the temperature change in the tumors was monitored via an infrared thermal camera. The tumor volume, survival ratio, and body weight were recorded every two days for 21 days thereafter. The tumor volume was calculated via the following formula:

$$\text{Tumor volume} = \text{tumor length} \times (\text{tumor width})^2 / 2 \quad (1).$$

Histopathology Analysis

The mice were sacrificed after 21 days, and the major organs and tumors were collected, fixed, embedded in paraffin, and subjected to H&E, TUNEL, and Ki67 staining. The histopathology images were investigated via optical microscopy.

Statistical Analysis

The data are presented as the means \pm standard deviations (SDs). The statistical significance was analyzed via one-way ANOVA via SPSS 22 (IBM SPSS Inc., Chicago, IL, USA). $P < 0.05$ was considered significant, and the data are denoted by * for $P < 0.05$, ** for $P < 0.01$, *** for $P < 0.001$, and **** for $P < 0.0001$.

Results and Discussion

The AuNRs were synthesized using a seed-mediated growth method and coated with a mesoporous PDA layer, enhancing the drug loading capacity of the AuNRs. DOX, a representative model drug, was then encapsulated within Au@mPDA through a π - π stacking interaction due to the phenolic groups present in both mPDA and DOX. The resulting Au@mPDA@DOX system can release DOX in response to photothermal effects and/or acidic conditions, facilitating a combined photothermal-chemotherapy approach for breast cancer treatment.

Initially, TEM and SEM were employed to examine the morphologies of Au and Au@mPDA. As shown in Figure 1A and B, the Au nanorods displayed good dispersion, with average dimensions of 123.84 ± 10.20 nm in length and 53.43 ± 4.20 nm in width. Following the coating with mPDA, the Au@mPDA exhibited core-shell and mesoporous structures, with the average size of the nanorods increasing to 195.11 ± 11.38 nm in length and 131.48 ± 6.10 nm in width, and the mPDA coating thickness was about 40 nm. Elemental mapping and EDS spectra of Au@mPDA demonstrated a uniform distribution of Au, C, N, and O, confirming the successful synthesis and distinct core-shell structure (Figure 1C and D). The Au nanorods showed a positive zeta potential of 20.13 ± 0.61 mV. However, after mPDA coating, the zeta potential shifted to a negative value of -11.83 ± 0.31 mV, potentially reducing nonspecific interactions with proteins (Figure 1E). The mesoporous structure of Au@mPDA also facilitated efficient drug loading and protection. Following DOX encapsulation, the zeta potential increased slightly to -5.15 ± 0.24 mV due to the positive charge of DOX. UV-Vis spectra further confirmed the mPDA coating and DOX encapsulation. The characteristic absorbance of the Au nanorods at about 758 nm redshifted to 855 nm after mPDA coating, enhancing NIR irradiation (Figure 1F). Additionally, the characteristic absorbance peak of DOX at 480 nm was observed in Au@mPDA@DOX, indicating successful encapsulation of DOX.

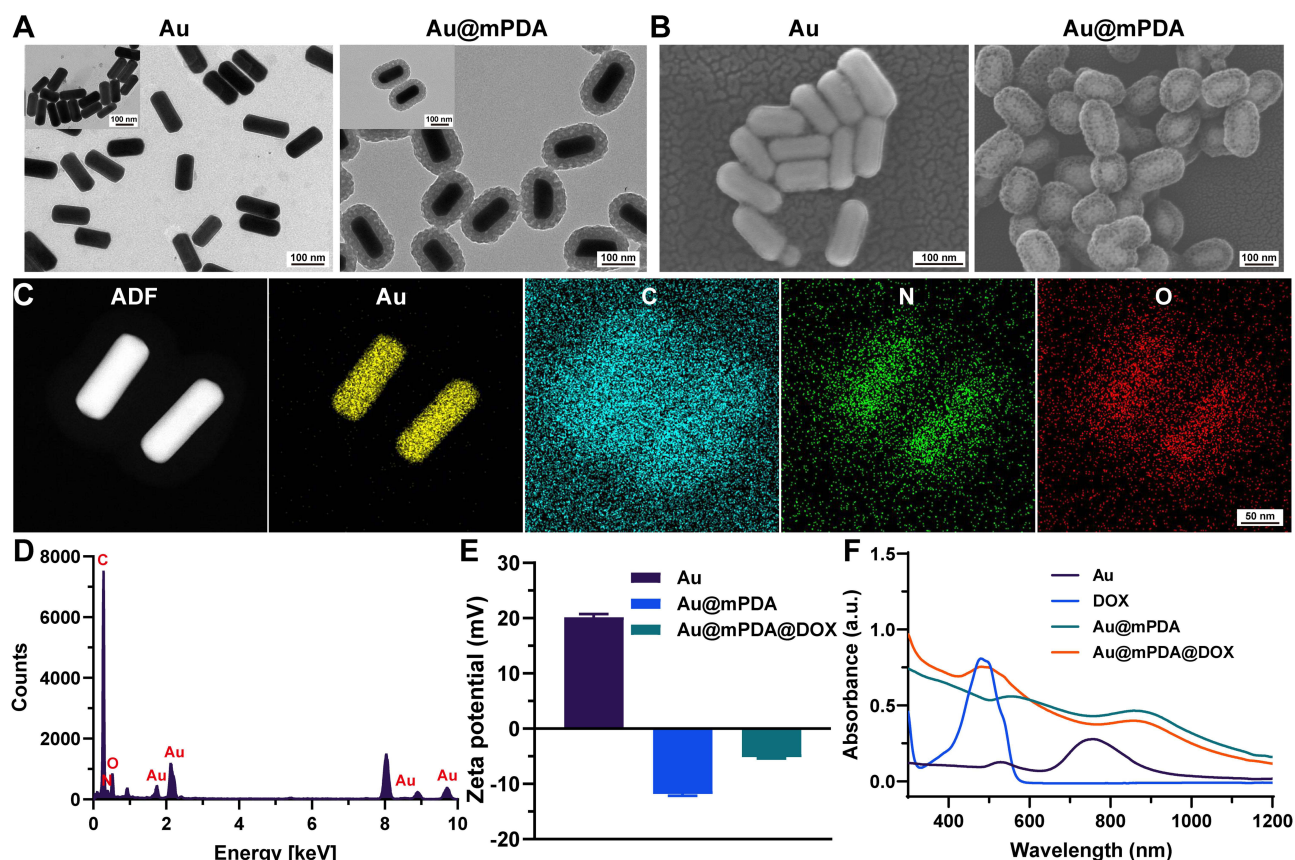


Figure 1 Characterization of the Au@mPDA@DOX nanoparticles. (A) TEM and (B) SEM images of Au and Au@mPDA. (C) Elemental mapping and (D) EDS spectrum of Au@mPDA@DOX. (E) Zeta potential of Au, Au@mPDA and Au@mPDA@DOX ($n = 3$). (F) UV-Vis spectra of Au, DOX, Au@mPDA, and Au@mPDA@DOX.

Owing to the strong absorbance of Au@mPDA at the NIR biowindow, we further confirmed the photothermal ability of Au@mPDA. As displayed in Figure 2A-C, Au@mPDA exhibited concentration- and power-density-dependent temperature changes. After irradiation, the temperature of Au@mPDA at a concentration of 50 $\mu\text{g/mL}$ increased by about 18.7 $^{\circ}\text{C}$, whereas that of H_2O at a power density of 0.3 W/cm^2 was only 1.3 $^{\circ}\text{C}$. The photothermal stability of Au@mPDA was subsequently investigated after one and five on-off cycles of laser irradiation. Au@mPDA showed a negligible change after laser irradiation, demonstrating its excellent photothermal stability (Figure 2D and E). In addition, chicken breast tissues of various thicknesses were used to simulate biological tissue to evaluate the tumor penetration of Au@mPDA. As shown in Figure S1, the temperature changes of the solutions were about 8.5 $^{\circ}\text{C}$ and 3.0 $^{\circ}\text{C}$ at depths of 2 mm and 8 mm, respectively. Collectively, these photothermal conversion abilities and stabilities of Au@mPDA provide promising avenues for further in vitro and in vivo photothermal therapy studies.

Responsive drug release profiles of DOX were recorded to prove the concept of on-demand therapy. As shown in Figure 3A, the amount of released DOX increased with decreasing pH. For example, in a physiological environment at pH 7.4, about 1.80 ± 0.20 μg of DOX was released after 48 h and increased to 4.13 ± 0.08 μg at pH 5.0, indicating that Au@mPDA@DOX was acid-sensitive. Additionally, after laser irradiation, the cumulative release of DOX was further increased under all conditions, with improvements of about 0.11 ± 0.01 , 0.22 ± 0.01 , and 0.28 ± 0.02 μg at pH 7.4, 6.2 and 5.0, respectively, which together indicate the pH- and irradiation-dependent release properties of Au@mPDA@DOX (Figure 3B).

We subsequently evaluated the cellular uptake ability of Au@mPDA@DOX in 4T1 cells using CLSM. As shown in Figure 3D and E, the fluorescence intensity of DOX gradually increased with time, indicating that the cellular uptake of Au@mPDA@DOX displayed positive time-dependent behavior. Interestingly, the fluorescence intensity of DOX reached a peak at 4 h post-treatment, and then decreased afterwards (Figure S2A and S2B). Notably, laser irradiation significantly enhanced the cellular uptake of DOX into 4T1 cells ($P < 0.05$) and increased the fluorescence of DOX distributed within the nucleus after laser treatment. This suggested that laser irradiation could be utilized to enhance the intracellular delivery of nanoparticles through increasing cell membrane permeability and endocytosis.⁴⁰

A hemolysis study and a CCK-8 assay were utilized to evaluate the in vitro cytotoxicity of Au@mPDA and Au@mPDA@DOX, respectively. A hemolysis study revealed that the hemolysis ratio was less than 5% after incubation

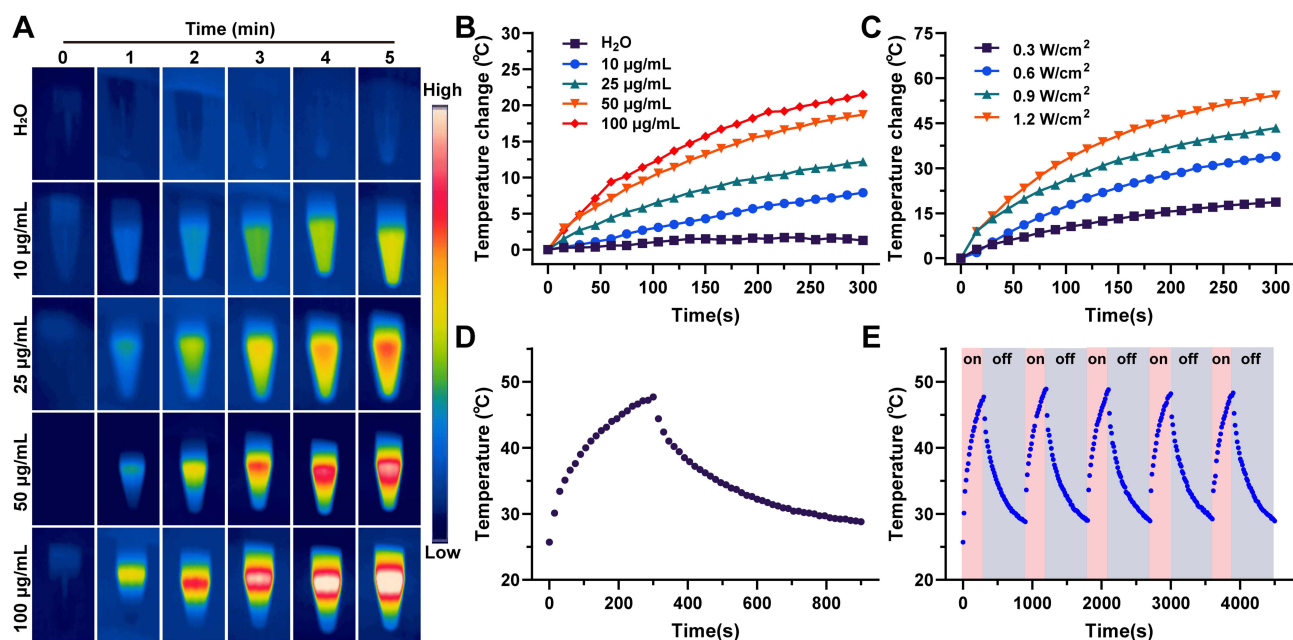


Figure 2 Photothermal conversion ability of Au@mPDA. (A) Photothermal images and (B) corresponding temperature change curves of Au@mPDA under 808-nm laser irradiation. (C) Temperature change curves of Au@mPDA at different laser powers. Photothermal stability of Au@mPDA after (D) one or (E) five on/off cycles of 808-nm laser irradiation.

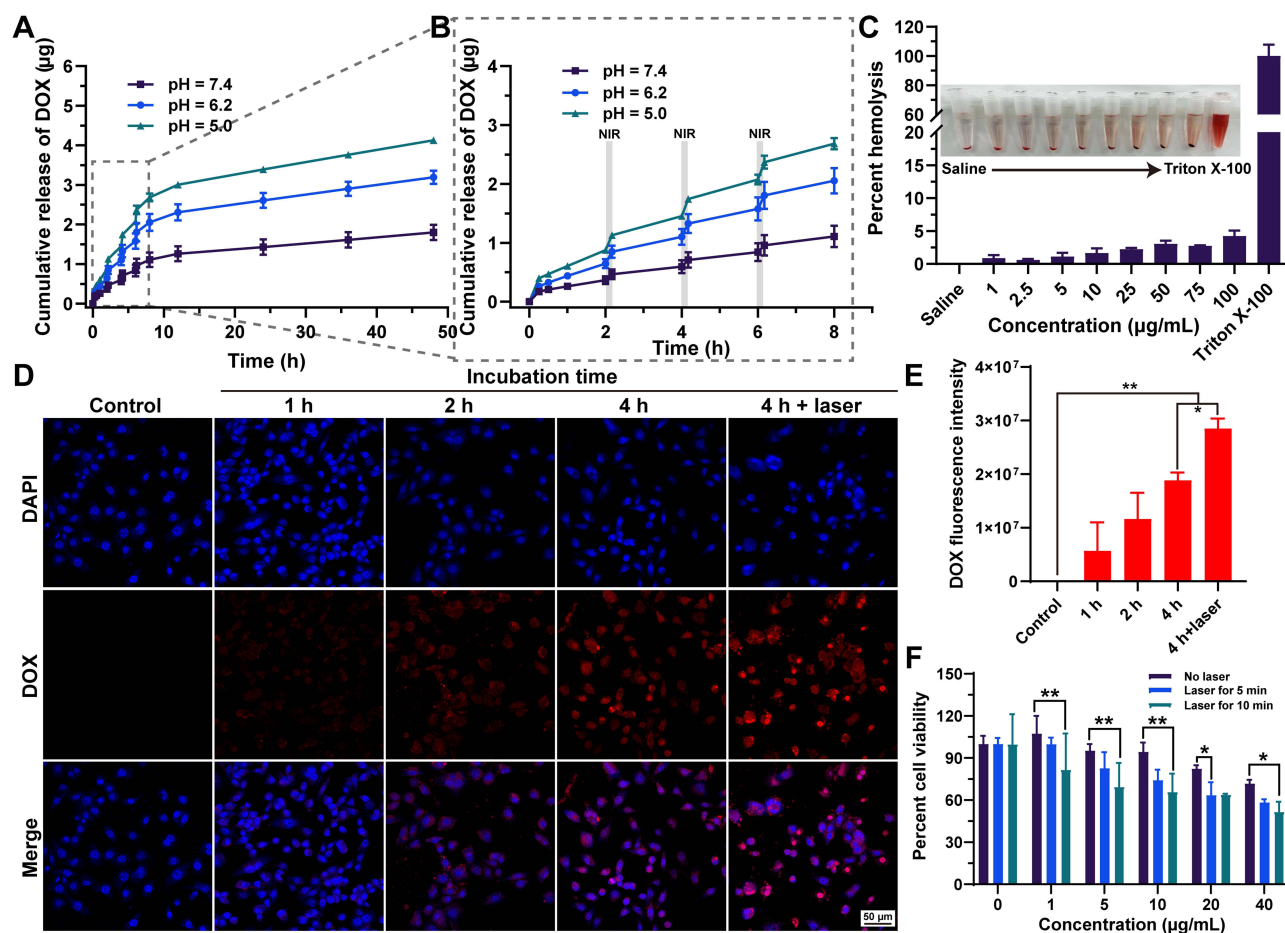


Figure 3 In vitro release, cytotoxicity and cellular uptake of Au@mPDA@DOX. (A) and (B) In vitro cumulative release of DOX from Au@mPDA@DOX under various conditions with or without laser irradiation ($n = 3$). (C) Hemolysis analysis of Au@mPDA at different concentrations. (D) CLSM images and (E) corresponding DOX fluorescence intensity of Au@mPDA@DOX after incubation with 4T1 cells for various durations. The data are presented as the mean \pm SD ($n = 3$). * $P < 0.05$, ** $P < 0.01$. (F) Cell viability of 4T1 cells after various laser treatments. The data are presented as mean \pm SD ($n = 4$).

with various concentrations of Au@mPDA, even at concentrations of up to 100 $\mu\text{g/mL}$, suggesting that the Au@mPDA possessed good biocompatibility (Figure 3C). A CCK-8 assay was conducted to explore the anti-tumor effects of Au@mPDA@DOX on 4T1 cells. After Au@mPDA@DOX treatment, the cell viability decreased with increasing concentration and decreased to $71.74 \pm 2.71\%$ at a concentration of 40 $\mu\text{g/mL}$. The similarly decreased cell viability trend could be observed after DOX and Au@mPDA treatment (Figure S2C and S2D). Furthermore, NIR irradiation further amplified the damage to 4T1 cells. After laser irradiation for 5 or 10 min, the cell viability decreased to $58.30 \pm 2.25\%$ and $51.85 \pm 6.90\%$, respectively, suggesting that the synergistic effects of combined photothermal chemotherapy could enhance the anti-tumor efficiency (Figure 3F).

A 4T1 tumor spheroid model was established to mimic solid tumors for the evaluation of tumor penetration. The DOX fluorescence at various depths in the tumor spheroids was scanned via CLSM after 4 or 8 h of incubation with or without laser irradiation to assess the deep penetration of Au@mPDA@DOX. As displayed in Figure 4A, the fluorescence intensity of DOX after 8 h of incubation was greater than that after 4 h of incubation at various depths. In addition, laser irradiation further increased the DOX fluorescence intensity after both 4 h and 8 h of incubation, and DOX fluorescence was observed in the core region at 20 μm . ROI quantification and 3D analysis of the images revealed that, at 8 h of incubation with laser irradiation, Au@mPDA@DOX had the strongest fluorescence intensity (Figure 4B). These results implied that the deep penetration of Au@mPDA@DOX was time- and laser irradiation-dependent and that laser irradiation enhanced the permeability and fluidity of the cell membranes via hyperthermia, which was coincident with the results of cellular uptake (Figure 3D and E).

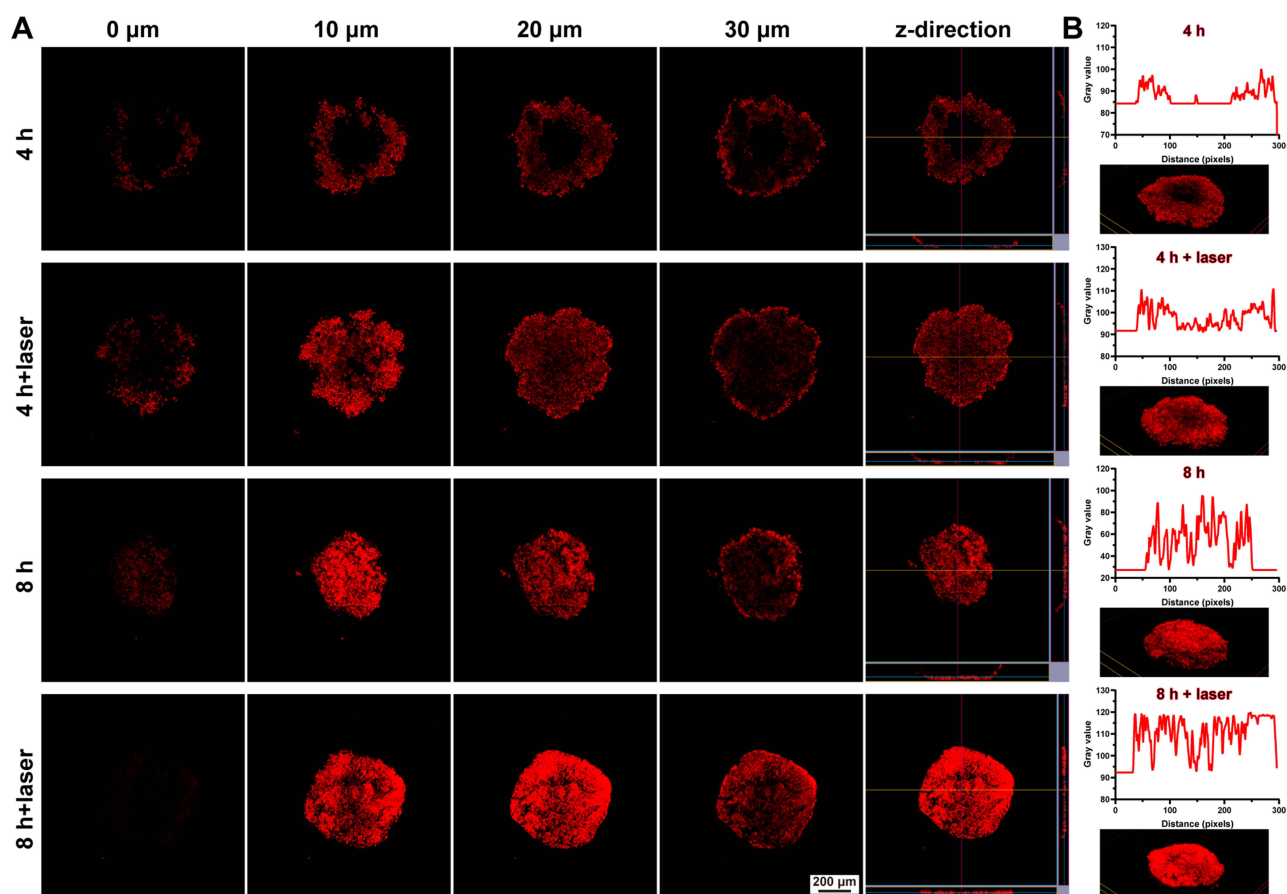


Figure 4 Deep penetration of 4T1 tumor spheroids by Au@mPDA@DOX. **(A)** Representative multilevel scan and **(B)** dynamic intensity of Au@mPDA@DOX penetration into 3D tumor spheroids after incubation for 4 or 8 h with or without laser irradiation.

Then, we evaluated the *in vitro* anti-tumor effects of Au@mPDA@DOX using live-cell staining and an Annexin V-APC/7-AAD apoptosis kit. First, Calcein-AM was used to stain live cells for green fluorescence after different treatments. As shown in Figures 5A and S3, the fluorescence of Calcein-AM slightly decreased after Au@mPDA@DOX treatment. After laser irradiation, the green fluorescence sharply decreased in both the Au@mPDA and the Au@mPDA@DOX groups, indicating that irradiation-mediated PTT enhanced the cell-killing ability of the nanoparticles. Compared with that of the Au@mPDA group, the green fluorescence of the cells decreased after the Au@mPDA@DOX treatment, further confirming that chemotherapy and PTT have synergistic anti-tumor effects.

Next, an Annexin V-APC/7-AAD apoptosis kit was used to evaluate the degree of apoptosis by flow cytometry. 4T1 cells were incubated with PBS, DOX, Au@mPDA, or Au@mPDA@DOX for 6 h with or without laser irradiation and then stained with Annexin V-APC and 7-AAD, which were defined as necrotic/late apoptotic cells. As shown in Figure 5B and C, the survival rates of the control and control + laser groups were greater than 90%, and negligible apoptotic signals were detected. In contrast, compared with PBS ($5.07 \pm 0.72\%$), DOX ($6.78 \pm 0.18\%$), or Au@mPDA ($9.07 \pm 2.46\%$), Au@mPDA@DOX increased the late apoptosis rate of cells ($9.75 \pm 1.20\%$). However, the combination of Au@mPDA@DOX with laser irradiation caused a strong increase in the percentage of late apoptotic cells to $15.44 \pm 3.61\%$. These results also suggested that Au@mPDA@DOX treatment combined with laser irradiation treatment could lead to late apoptosis of cancer cells, which was consistent with the outcomes of the live-cell staining assay, confirming that Au@mPDA@DOX exerted satisfactory *in vitro* anti-tumor effects via a synergistic optical strategy for combined photothermal chemotherapy against breast cancer. The ability of the nanoparticles to inhibit migration was also evaluated via a scratch assay. Owing to the strong metastatic characteristics of the 4T1 cells, the control group had the greatest

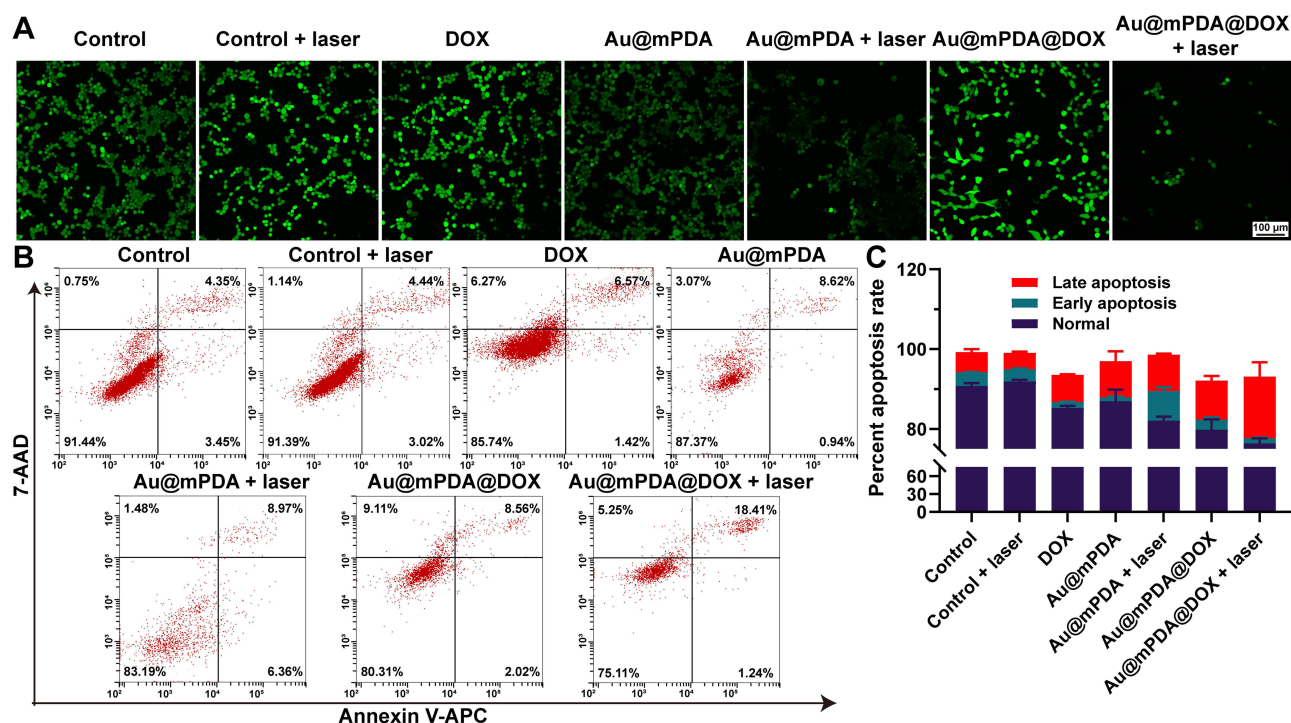


Figure 5 In vitro evaluation of the antitumor effect on 4T1 cells. **(A)** Calcein-AM staining of cells after various treatments. **(B)** Assessment of cell apoptosis by flow cytometric analysis and **(C)** its quantification. The data are presented as mean \pm SD ($n = 3$).

degree of wound healing ($28.29 \pm 9.47\%$) compared with the DOX ($17.93 \pm 14.94\%$) and Au@mPDA@DOX ($12.21 \pm 2.53\%$) treatment groups (Figure S4). The number of cells incubated with Au@mPDA@DOX with the addition of laser irradiation decreased to $7.40 \pm 1.69\%$, suggesting that the combination of PTT and chemotherapy strongly inhibited cell metastasis.

As a typical NIR probe, ICG is more sensitive as a fluorescence probe than is DOX for in vivo fluorescence imaging.⁴⁵ Hence, ICG was employed to label the Au@mPDA nanoparticles in place of DOX. A live imaging system was utilized to investigate the real-time performance at various time intervals. As shown in Figure 6A and C, the fluorescence signal of ICG increased with time. It peaked at 2 h and then decreased, probably due to drug metabolism. The ICG fluorescence signal could also be visualized at the tumor site at 24 h post-injection, suggesting the tumor-targeting ability of Au@mPDA@ICG. At 24 h post-injection, the major organs and tumors of the mice were collected for ex vivo fluorescence imaging. The results of fluorescence imaging and semiquantitative analysis are displayed in Figure 6B and D. ICG fluorescence signals were highly accumulated in the liver, followed by the tumor, lung, and kidney, possibly because of drug capture by the reticuloendothelial system (RES).⁴⁶ The in vivo tumor penetration capability of Au@mPDA@ICG was assessed by embedding tumor tissues in optimal cutting temperature compound and sectioning, followed by CD31 staining for tumor growth investigation (green). As shown in Figure S5, ICG fluorescence was detected at depths up to 400 μm , further confirming the tumor-targeting and tumor depth penetration efficacy of Au@mPDA@ICG.

On the basis of the in vivo fluorescence results, a photothermal imaging assay was performed after intravenous injection of saline, Au@mPDA or Au@mPDA@DOX into the mice for 2 h. An infrared camera was used to capture photothermal images of the mice to monitor the real-time temperature changes at the tumor site. As shown in Figure 6E and F, the temperature of the tumor tissue increased with increasing laser irradiation time and rapidly increased to 20.8°C within 10 min of irradiation in the Au@mPDA@DOX group, whereas it was only 16.5°C in the Au@mPDA group and 10.1°C in the control group, suggesting the effective photothermal conversion property of Au@mPDA@DOX.

An in vivo anti-tumor study was performed following the experimental protocol shown in Figure 7A. The tumor volume, body weight, and survival ratio were recorded during the treatment. Once the tumor volume exceeded

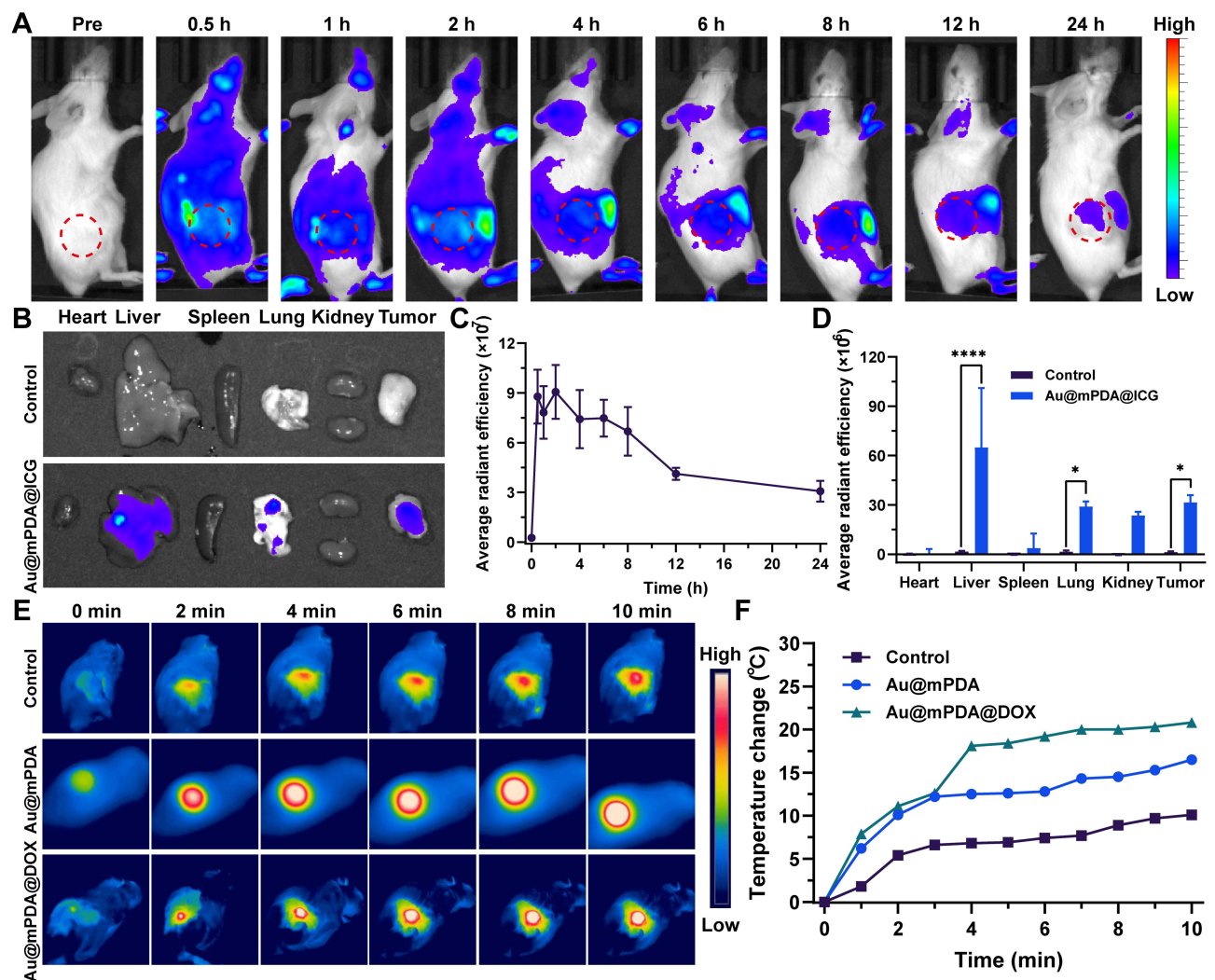


Figure 6 In vivo and ex vivo fluorescence and photothermal imaging. **(A)** In vivo fluorescence images and **(C)** average radiant efficiency of Au@mPDA@ICG in 4T1 tumor-bearing mice at 0, 0.5, 1, 2, 4, 6, 8, 12, and 24 h after injection. The tumors are labeled with red circles. **(B)** Ex vivo fluorescence imaging and **(D)** average radiant efficiency of major organs and tumors at 24 h. **(E)** NIR thermal images and **(F)** temperature changes in tumor sites treated with saline, Au@mPDA, or Au@mPDA@DOX with 808-nm laser irradiation. The data are presented as mean \pm SD ($n = 3$). * $P < 0.05$, **** $P < 0.0001$.

2000 mm³, the mice were defined as dead according to animal ethics. As shown in Figures 7B, C and S6, the tumor growth curves of the saline group rapidly increased throughout the entire experiment. The mice in the DOX, Au@mPDA, or Au@mPDA@DOX treatment groups presented tumor growth profiles analogous to those of the saline group and exhibited no obvious suppressive effect on tumor growth but only prolonged the survival ratio of the mice (Figure 7D). However, the mice treated with Au@mPDA or Au@mPDA@DOX with laser irradiation exhibited significant tumor inhibition ($P < 0.001$). Compared with the mice in the Au@mPDA plus laser irradiation group, the mice in the Au@mPDA@DOX plus laser irradiation group presented enhanced inhibitory effects, and tumors were negligible on day 13. In addition, the survival ratio of Au@mPDA@DOX after laser irradiation was greater than that of Au@mPDA with irradiation, suggesting that synergistic therapy of photothermal and chemotherapy could effectively enhance the anti-tumor effects and prolong the survival period. The body weights of the mice subjected to various treatments did not obviously change during the treatment period, indicating the good biosafety of either Au@mPDA or Au@mPDA@DOX (Figure 7E).

To further assess the anti-tumor effect of Au@mPDA@DOX, after various treatments, tumors were collected for histopathological analysis by H&E, TUNEL, and Ki67 staining. Compared with those in the other groups, the tumors in the Au@mPDA@DOX plus laser irradiation group presented more severe vacuolization and necrosis, as shown by H&E

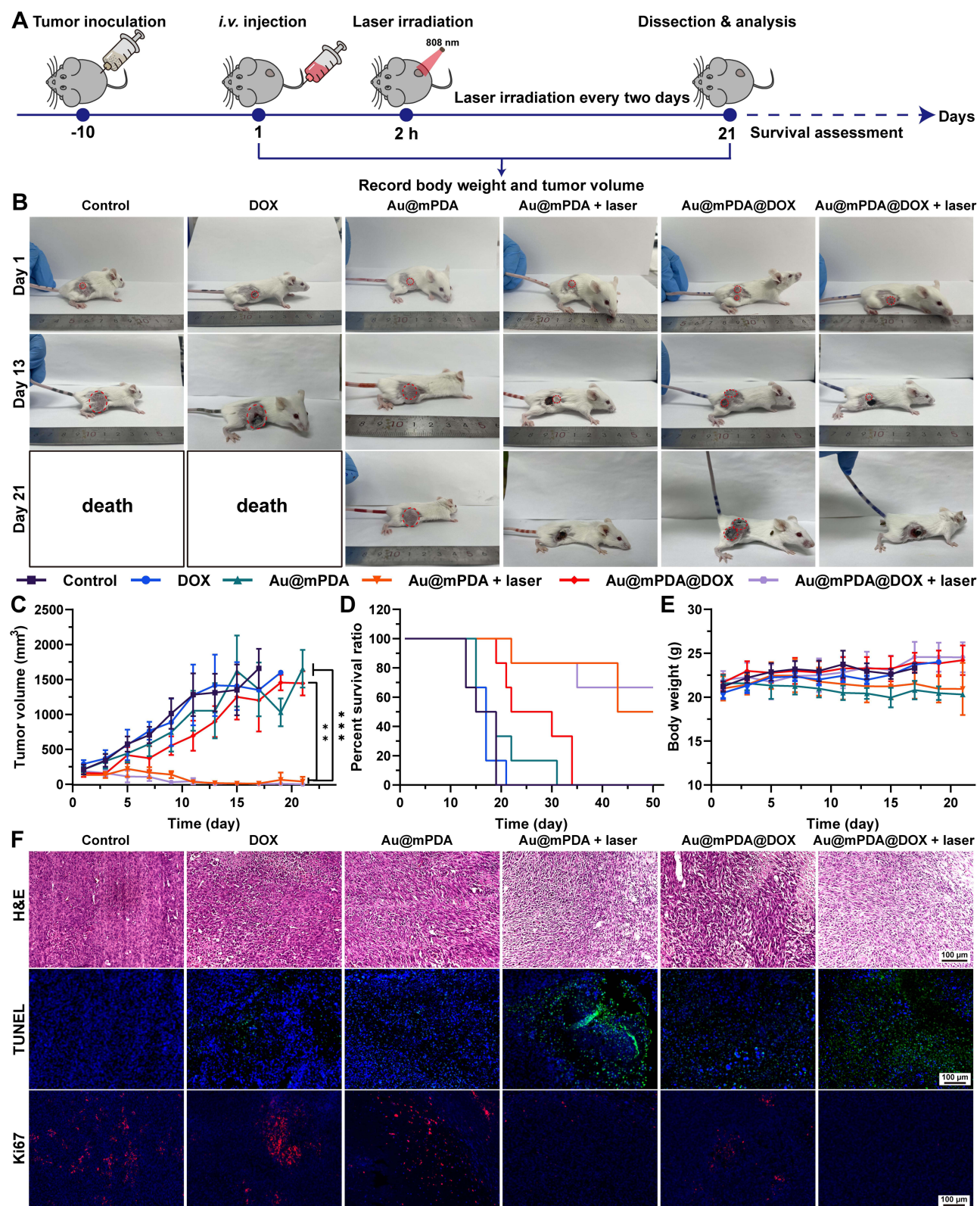


Figure 7 In vivo pharmacodynamics study. **(A)** Schematic illustration of the therapeutic protocol. **(B)** Photographs of the mice on Days 1, 13, and 21. The tumor is labeled with red circles. **(C)** Tumor volume, **(D)** survival ratio and **(E)** body weight of the mice after saline, DOX, Au@mPDA, Au@mPDA + laser, Au@mPDA@DOX, or Au@mPDA@DOX + laser treatments. The data are presented as mean \pm SD ($n = 6$). $**P < 0.01$, $***P < 0.001$. **(F)** H&E, TUNEL, and Ki67 staining of tumor slices from different groups of mice.

staining (Figures 7F, S7 and S8). Moreover, immunofluorescent TUNEL and Ki67 staining were used to detect the degree of apoptosis and proliferation, respectively, of the tumor cells. The images showed that, relative to other groups, the Au@mPDA@DOX plus laser irradiation group exhibited a higher number of TUNEL-positive cells and a lower number of Ki67-positive cells, suggesting that the combination of chemotherapy and PTT effectively induced tumor cell apoptosis and suppressed tumor cell proliferation. Furthermore, no significant damage was detected in major organs, including the heart, liver, spleen, lung, and kidney, which were stained with H&E (Figure S9). These findings indicate that the synergistic optical strategy of combined photothermal and chemotherapy significantly enhances anti-tumor effects against breast cancer in mice model.

Conclusion

Overall, we successfully constructed a core-shell nanoplatform (Au@mPDA@DOX) combined with DOX-mediated chemotherapy and Au@mPDA-mediated PTT to fight against breast cancer in mice model. The tailored Au@mPDA@DOX displayed excellent photothermal properties and pH/photothermal dual-responsive drug release performance. After injection, Au@mPDA@DOX passively targeted the tumor site via the EPR effect and exhibited improved anti-tumor effects via not only PTT-induced thermal ablation but also enhanced the cellular uptake and penetration depth of DOX owing to synergistic PTT-mediated hyperthermia. This nanoplatform, which integrates chemotherapy and PTT technologies, could expand its applications in pharmacotherapy against other diseases. First, the excellent photothermal conversion ability of the AuNRs allows them to penetrate deeply into tumor sites at relatively high temperatures, leading to the on-demand controlled release of drugs and tumor ablation. Second, the mesoporous structures of mPDA largely facilitated the drug loading encapsulation. Finally, Au@mPDA can be employed as a promising nanocarrier for targeted drug delivery and photothermal imaging. Our study thus provides a promising approach as a synergistic and optical strategy to combined photothermal chemotherapy for breast cancer treatment. Despite the ideal tumor-targeting and anti-tumor effects of Au@mPDA@DOX both in vitro and in vivo, the drugs were distributed mainly in the liver, followed by the tumor and the lung. This necessitates further enhancement of the targeting ability and evaluation of the long-term toxicity of our drug delivery system in the future.

Abbreviations

DOX, doxorubicin; NDDSs, nano-drug delivery systems; EPR, enhanced permeability and retention; PTT, photothermal therapy; Au, gold; AuNRs, Au nanorods; LSPR, localized surface plasmon resonance; mPDA, mesoporous polydopamine; NIR, near-infrared; $\text{HAuCl}_4 \cdot 3\text{H}_2\text{O}$, hydrogen tetrachloroaurate (III) trihydrate; CTAB, hexadecyl trimethyl ammonium bromide; AgNO_3 , silver nitrate; NaBH_4 , hydroquinone, sodium borohydride; DA·HCl, dopamine hydrochloride; DOX·HCl, doxorubicin hydrochloride; TMB, 1,3,5-Trimethylbenzene; $\text{NH}_3 \cdot \text{H}_2\text{O}$, Ammonia aqueous solution; TEM, transmission electronic microscopy; SEM, scanning electron microscopy; EDS, energy dispersive X-ray spectroscopy; CLSM, confocal laser scanning microscope; RBCs, red blood cells; 3D, three-dimensional; ICG, indocyanine green; IVIS, in vivo imaging system; SD, standard deviation; RES, reticuloendothelial system.

Acknowledgments

This research was funded by the Zhejiang Provincial Natural Science Foundation of China (LQ23H300001), the Research Project of Zhejiang Chinese Medical University (2023JKZDZC03 and 2022JKJNTZ12), and the Science and Technology Innovation Team Project of Zhejiang Province (2023R410005). We appreciate the great experimental support from the Medical Research Center, Academy of Chinese Medical Sciences, Zhejiang Chinese Medical University.

Disclosure

The authors declare no conflicts of interest in this work.

References

1. Siegel RL, Miller KD, Wagle NS, Jemal A. Cancer statistics, 2023. *CA-Cancer J Clin*. 2023;73(1):17–48. doi:10.3322/caac.21763
2. Trapani D, Ginsburg O, Fadelu T, et al. Global challenges and policy solutions in breast cancer control. *Cancer Treat Rev*. 2022;104:102339. doi:10.1016/j.ctrv.2022.102339
3. Alamdari SG, Amini M, Jalilzadeh N, et al. Recent advances in nanoparticle-based photothermal therapy for breast cancer. *J Control Release*. 2022;349:269–303. doi:10.1016/j.jconrel.2022.06.050
4. Hao W, Zheng Z, Zhu L, et al. 3D printing-based drug-loaded implanted prosthesis to prevent breast cancer recurrence post-conserving surgery. *Asian J Pharm Sci*. 2021;16(1):86–96. doi:10.1016/j.ajps.2020.06.002
5. Zangouei AS, Alimardani M, Moghbeli M. MicroRNAs as the critical regulators of doxorubicin resistance in breast tumor cells. *Cancer Cell Int*. 2021;21(1):213. doi:10.1186/s12935-021-01873-4
6. Nicoletto RE, Ofner CM. Cytotoxic mechanisms of doxorubicin at clinically relevant concentrations in breast cancer cells. *Cancer Chemoth Pharm*. 2022;89(3):285–311. doi:10.1007/s00280-022-04400-y
7. Wang C, Li N, Li Y, et al. Engineering a HEK-293T exosome-based delivery platform for efficient tumor-targeting chemotherapy/internal irradiation combination therapy. *J Nanobiotechnol*. 2022;20(1):247. doi:10.1186/s12951-022-01462-1
8. Meng L, Chu X, Xing H, et al. Improving glioblastoma therapeutic outcomes via doxorubicin-loaded nanomicelles modified with borneol. *Int J Pharm*. 2019;567:118485. doi:10.1016/j.ijpharm.2019.118485
9. Solanki R, Jodha B, Prabina KE, Aggarwal N, Patel S. Recent advances in phytochemical based nano-drug delivery systems to combat breast cancer: a review. *J Drug Deliv Sci Tec*. 2022;77:103832. doi:10.1016/j.jddst.2022.103832
10. Malik JA, Ansari JA, Ahmed S, Khan A, Ahemad N, Anwar S. Nano-drug delivery system: a promising approach against breast cancer. *Ther deliv*. 2023;14(5):357–381. doi:10.4155/tde-2023-0020
11. Duan L, Yang L, Jin J, et al. Micro/nano-bubble-assisted ultrasound to enhance the EPR effect and potential theranostic applications. *Theranostics*. 2020;10(2):462–483. doi:10.7150/thno.37593
12. Kalyane D, Raval N, Maheshwari R, Tambe V, Kalia K, Tekade RK. Employment of enhanced permeability and retention effect (EPR): nanoparticle-based precision tools for targeting of therapeutic and diagnostic agent in cancer. *Mater Sci Eng C-Mater*. 2019;98:1252–1276. doi:10.1016/j.msec.2019.01.066
13. Golombek SK, May J-N, Theek B, et al. Tumor targeting via EPR: strategies to enhance patient responses. *Adv Drug Deliv Rev*. 2018;130:17–38. doi:10.1016/j.addr.2018.07.007
14. Yu M, Zheng J. Clearance pathways and tumor targeting of imaging nanoparticles. *ACS Nano*. 2015;9(7):6655–6674. doi:10.1021/acsnano.5b01320
15. Li L, ten Hagen TLM, Bolkestein M, et al. Improved intratumoral nanoparticle extravasation and penetration by mild hyperthermia. *J Control Release*. 2013;167(2):130–137. doi:10.1016/j.jconrel.2013.01.026
16. Hu Q, Sun W, Wang C, Gu Z. Recent advances of cocktail chemotherapy by combination drug delivery systems. *Adv Drug Deliv Rev*. 2016;98:19–34. doi:10.1016/j.addr.2015.10.022
17. Chen H, Sun R, Zheng J, Kawazoe N, Yang Y, Chen G. Doxorubicin-encapsulated thermosensitive liposome-functionalized photothermal composite scaffolds for synergistic photothermal therapy and chemotherapy. *J Mat Chem B*. 2022;10(25):4771–4782. doi:10.1039/d2tb00993e
18. Xin Z, Shen Y, Hao H, Zhang L, Hu X, Wang J. Hyaluronic acid coated mesoporous carbon-copper peroxide for H₂O₂ self-supplying and near-infrared responsive multi-mode breast cancer oncotherapy. *Colloids Surf B*. 2022;218:112776. doi:10.1016/j.colsurfb.2022.112776
19. Tang Y, Liao X, Wang C, et al. Self-assembled small messenger RNA nanospheres for efficient therapeutic apoptin expression and synergistic gene-chemotherapy of breast cancer. *J Colloid Interface Sci*. 2021;603:191–198. doi:10.1016/j.jcis.2021.06.061
20. Chen J, Ning C, Zhou Z, et al. Nanomaterials as photothermal therapeutic agents. *Prog Mater Sci*. 2019;99:1–26. doi:10.1016/j.pmatsci.2018.07.005
21. Zhao Y, Liu N, Liu P, et al. Robust boron nanoplatform provokes potent tumoricidal activities via inhibiting heat shock protein. *Asian J Pharm Sci*. 2022;17(5):728–740. doi:10.1016/j.ajps.2022.06.003
22. Cheng Y, Bao D, Chen X, et al. Microwave-triggered/HSP-targeted gold nano-system for triple-negative breast cancer photothermal therapy. *Int J Pharm*. 2021;593:120162. doi:10.1016/j.ijpharm.2020.120162
23. Piao J-G, Wang L, Gao F, You Y-Z, Xiong Y, Yang L. Erythrocyte membrane is an alternative coating to polyethylene glycol for prolonging the circulation lifetime of gold nanocages for photothermal therapy. *ACS Nano*. 2014;8(10):10414–10425. doi:10.1021/nn503779d
24. Wang J, Zhang Y, Jin N, Mao C, Yang M. Protein-induced gold nanoparticle assembly for improving the photothermal effect in cancer therapy. *ACS Appl Mater Interfaces*. 2019;11(12):11136–11143. doi:10.1021/acsami.8b21488
25. Dong Z, Gong H, Gao M, et al. Polydopamine nanoparticles as a versatile molecular loading platform to enable imaging-guided cancer combination therapy. *Theranostics*. 2016;6(7):1031–1042. doi:10.7150/thno.14431
26. Lu J, Cai L, Dai Y, et al. Polydopamine-based nanoparticles for photothermal therapy/chemotherapy and their synergistic therapy with autophagy inhibitor to promote antitumor treatment. *Chem Rec*. 2021;21(4):781–796. doi:10.1002/tcr.202000170
27. Liu X, Liu Y, Guo Y, et al. Metabolizable pH/H₂O₂ dual-responsive conductive polymer nanoparticles for safe and precise chemo-photothermal therapy. *Biomaterials*. 2021;277:121115. doi:10.1016/j.biomaterials.2021.121115
28. Feng S, Lu J, Wang K, et al. Advances in smart mesoporous carbon nanoplatforms for photothermal-enhanced synergistic cancer therapy. *Chem Eng J*. 2022;435:134886. doi:10.1016/j.cej.2022.134886
29. Yang K, Wan J, Zhang S, Tian B, Zhang Y, Liu Z. The influence of surface chemistry and size of nanoscale graphene oxide on photothermal therapy of cancer using ultra-low laser power. *Biomaterials*. 2012;33(7):2206–2214. doi:10.1016/j.biomaterials.2011.11.064
30. Xu C, Pu K. Second near-infrared photothermal materials for combinational nanotheranostics. *Chem Soc Rev*. 2021;50(2):1111–1137. doi:10.1039/d0cs00664e
31. Tabish TA, Dey P, Mosca S, et al. Smart gold nanostructures for light mediated cancer theranostics: combining optical diagnostics with photothermal therapy. *Adv Sci*. 2020;7(15):1903441. doi:10.1002/advs.201903441
32. Li W, Cao Z, Yu L, et al. Hierarchical drug release designed Au @PDA-PEG-MTX NPs for targeted delivery to breast cancer with combined photothermal-chemotherapy. *J Nanobiotechnol*. 2021;19(1):143. doi:10.1186/s12951-021-00883-8

33. Alle M, Sharma G, Lee S-H, Kim J-C. Next-generation engineered nanogold for multimodal cancer therapy and imaging: a clinical perspectives. *J Nanobiotechnol.* 2022;20(1):222. doi:10.1186/s12951-022-01402-z
34. Ye L, Chen Y, Mao J, Lei X, Yang Q, Cui C. Dendrimer-modified gold nanorods as a platform for combinational gene therapy and photothermal therapy of tumors. *J Exp Clin Canc Res.* 2021;40(1):303. doi:10.1186/s13046-021-02105-3
35. Xu W, Qian J, Hou G, et al. Hyaluronic acid-functionalized gold nanorods with pH/NIR dual responsive drug release for synergetic targeted photothermal chemotherapy of breast cancer. *ACS Appl Mater Interfaces.* 2017;9(42):36533–36547. doi:10.1021/acsami.7b08700
36. Yang Y, Lin Y, Di D, et al. Gold nanoparticle-gated mesoporous silica as redox-triggered drug delivery for chemo-photothermal synergistic therapy. *J Colloid Interface Sci.* 2017;508:323–331. doi:10.1016/j.jcis.2017.08.050
37. Zhang Z, Wang L, Wang J, et al. Mesoporous silica-coated gold nanorods as a light-mediated multifunctional theranostic platform for cancer treatment. *Adv Mater.* 2012;24(11):1418–1423. doi:10.1002/adma.201104714
38. Zhang L, Chen S, Ma R, et al. NIR-excitable PEG-modified au nanorods for photothermal therapy of cervical cancer. *ACS Appl Nano Mater.* 2021;4(12):13060–13070. doi:10.1021/acsanm.1c02594
39. Wu D, Zhou J, Chen X, et al. Mesoporous polydopamine with built-in plasmonic core: traceable and NIR triggered delivery of functional proteins. *Biomaterials.* 2020;238:119847. doi:10.1016/j.biomaterials.2020.119847
40. Sherlock SP, Tabakman SM, Xie L, Dai H. Photothermally enhanced drug delivery by ultrasmall multifunctional FeCo/Graphitic shell nanocrystals. *ACS Nano.* 2011;5(2):1505–1512. doi:10.1021/nn103415x
41. Sun H, Zhang Q, Li J, Peng S, Wang X, Cai R. Near-infrared photoactivated nanomedicines for photothermal synergistic cancer therapy. *Nano Today.* 2021;37:101073. doi:10.1016/j.nantod.2020.101073
42. Wu D, Zhou J, Creyer MN, et al. Phenolic-enabled nanotechnology: versatile particle engineering for biomedicine. *Chem Soc Rev.* 2021;50(7):4432–4483. doi:10.1039/d0cs00908c
43. Wu D, Chen X, Zhou J, et al. A synergistic optical strategy for enhanced deep-tumor penetration and therapy in the second near-infrared window. *Mater Horiz.* 2020;7(11):2929–2935. doi:10.1039/d0mh00870b
44. Chen B, Mei L, Fan R, et al. Polydopamine-coated i-motif DNA/Gold nanoplateforms for synergistic photothermal- chemotherapy. *Asian J Pharm Sci.* 2023;18(2):100781. doi:10.1016/j.ajps.2023.100781
45. Chen X, Zou J, Zhang K, et al. Photothermal/matrix metalloproteinase-2 dual-responsive gelatin nanoparticles for breast cancer treatment. *Acta Pharm Sin B.* 2021;11(1):271–282. doi:10.1016/j.apsb.2020.08.009
46. Liu T, Choi H, Zhou R, Chen IW. RES blockade: a strategy for boosting efficiency of nanoparticle drug. *Nano Today.* 2015;10(1):11–21. doi:10.1016/j.nantod.2014.12.003

International Journal of Nanomedicine

Dovepress

Publish your work in this journal

The International Journal of Nanomedicine is an international, peer-reviewed journal focusing on the application of nanotechnology in diagnostics, therapeutics, and drug delivery systems throughout the biomedical field. This journal is indexed on PubMed Central, MedLine, CAS, SciSearch®, Current Contents®/Clinical Medicine, Journal Citation Reports/Science Edition, EMBase, Scopus and the Elsevier Bibliographic databases. The manuscript management system is completely online and includes a very quick and fair peer-review system, which is all easy to use. Visit <http://www.dovepress.com/testimonials.php> to read real quotes from published authors.

Submit your manuscript here: <https://www.dovepress.com/international-journal-of-nanomedicine-journal>